Electronic Supplementary Information (ESI)

Spin-induced Magnetic Anisotropy in novel Co-doped GaN Nano-needles and their related Photoluminescence

Muhammad Umair Farooq[a], Zhao Duan[a], Muhammad Ismail Farooq[a], Khushbu Fatima[b], Muhammad Abubaker khan[c], Zhang Li[a], Yuting Liu[a], Muhammad Yousaf[d], Bingsuo Zou[a]*

[a] Beijing Key Laboratory of Nanophotonics and Ultrafine Optoelectronic Systems, School of Physics, Beijing Institute of Technology, Beijing100081, China.

[b]Programme implementation unit, Inclusive voucher scheme, Special education department, Government of Punjab, Pakistan

[c]Beijing Key Laboratory of Science and Technology of Materials under Shock and Impact, School of Materials Science and Engineering, Beijing Institute of Technology, Beijing100081, China.

[d]Department of Materials Science and Engineering, College of Engineering, Peking University, Beijing 100871, China

*Correspondence: Bingsuo Zou; zoubs@bit.edu.cn ; Tel.: +86(10)6891-8188

Experimental Detail

Highly crystalline Co-doped GaN nanoneedles were synthesized by typical chemical vapor deposition (CVD) method in a horizontal furnace system. Well-mixed Ga_2O_3 (99.99%, Aladdin) and Co_3O_4 (Alfa Aesar, 99.9%) powders with the equimolar ratio (0.1:0.05 g) and carbon (0.07 g) were taken into a ceramic boat and heated up to 130 °C in a heating oven. Carbon was used as oxygen removal agent by forming CO/Co_2 at the low-temperature zone. It also helps to avoid to form metal agglomeration or cluster for the growth of TM doped semiconductor nanowires. Then it was agitated into glass rod after adding some drops of aqueous ammonia. This process was repeated three times after each 30 minutes interval, so-called pre-treatment. Pre-treatment of precursor with aqueous NH_3 provides the favorable sites and defect-free growth. After the pretreatment, several pieces of mica substrates were ultrasonically cleaned in acetone, ethanol, and deionized water for 15 min, coated with 10 nm thick gold film at room temperature by thermal beam evaporation system and placed into a horizontal tube furnace. Before the growth process, a mixture of Ar 90% and H_2 10% gases at 15 SCCM (standard cubic centimeters per minutes) was used for 25 minutes to derive out the air. Ammonia gas (99.999%) was introduced into quartz tube for 2 h with Ar + H_2 gas during the whole reaction process. The flow rate of NH_3 and mixed Ar gas was adjusted to 15 sccm and 15 sccm, respectively. The furnace was rapidly heated to 1100 ºC and maintained for about 120 min. The substrate temperature also has an effect on doping and Hc as well. For the cause, it provides enough energy to recognize the crystal growth and stability of dopant in the host alloy. Therefore, doping can be easily achieved at higher substrate temperature. In the case of GaN, growth is only possible at high temperature; further increasing substrate temperature may cause ejection of dopant from host alloy. After the reaction, the furnace was cooled down to room temperature under Ar gas flow and a yellow like product could be found on the surface of substrates.

During the growth mechanism, initially rise in temperature reduces the adhesion in the gold film because Au has less melting point and decomposes into nanometer-sized Au particle that was used as a catalyst. When the temperature approaches to 1100 °C, GaN

precursor decomposes into Ga and N vapors. These gaseous atoms might have been absorbed by Au nanoparticle as favorable energy sites to form GaN NNs. Whereas, NH_3 gas was used as nitriding and reaction agent for converting Ga vapors into GaN NNs.

The crystal structure investigation was carried out by using X-ray powder diffraction (XRD Philips X'Pert Pro MPD with Cu-Kα radiation source (λ = 0.15418 nm). The surface morphology was analyzed by a scanning electron microscope (SEM Zeiss Supra 55) and a transmission electron microscopy (TEM FEI Tecnai T20 and F30). Elemental composition
analysis of the as-synthesised product was determined by X-ray photo-electron spectroscopy (XPS, Kratos Axis Ultra with monochromatized Al Kα radiation (1486.6 eV) and energy dispersive X-ray spectroscopy (EDX). Magnetic properties were measured by employing a vibrating sample magnetometer (VSM Lakeshore 7407) and superconducting quantum interference device (MPMS SQUID). Raman scattering with 532 nm line of Ar+ was utilized to record the micro-Raman experiment equipped with an optical microscope (Olympus BX51M). Photoluminescence (PL) properties were studied by using UV light with excitation wavelength 325 nm He-Cd laser.

The possible chemical reactions that take part in the growth of GaN can be followed:

$$Ga_2O_3(s) + 3C(s) + 2NH_3(g) \rightarrow 2GaN(s) + 3H_2(v) + 3CO(v)_1 \quad (1)$$

$$Ga_2O_3(s) + 3C(s) \rightarrow Ga\,O(v) + 2Co(v)^2 \quad (2)$$

$$Ga_2O(v) + NH_{3(g)} \rightarrow 2GaN(s) + H_2O(v) + 2H_{2(v)}{}^{2,3} \quad (3)$$

The equations (3) and (4) reveal that during the growth process of GaN within NH_3 environment, Ga_2O_3 further reacts with H_2 to form Ga metal at the same time.

$$Ga_2O(v) + H_{2(g)} \rightarrow 2Ga(l) + H_2O(v)_3 \quad (4)$$

$$2Ga(l) + NH_{3(g)} \rightarrow 2GaN(s) + 2H_{2(g)}{}^3 \quad (5)$$

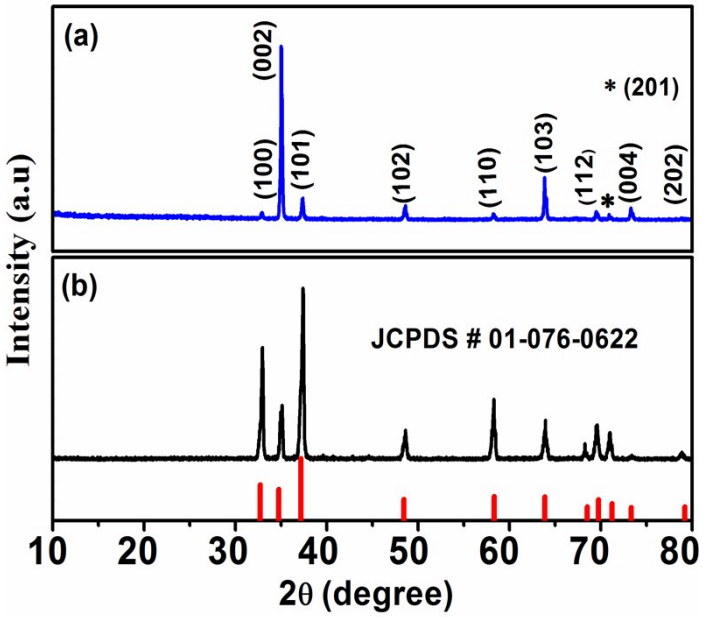

Figure S1. XRD pattern of as-synthesized (a) Co-doped GaN and (b) undoped GaN NNs.

The XRD analysis has been performed to investigate the crystal structure and phase purity of undoped and Co-doped GaN nanoneedles deposited on mica substrates. The indexed diffraction peaks corresponding to planes (100), (002), (101), (102), (110), (103), (112), (201) and (202) were observed as shown in (Fig. S1), indicating the formation of pure hexagonal wurtzite structure of GaN which is in good agreement with JCPDS card reference code: 01-076-0622. The strong and sharp peak at about $2\theta = 37.3°$ related to (002) plane of GaN indicates that Co-doped GaN nanoneedles are preferentially oriented along (002) direction. The diffraction intensities of the doped sample are weaker as compared to undoped GaN nanoneedles (NNs) confirming the Co concentration slightly impede the GaN crystallinity. Moreover, no typical secondary phases or crystalline impurity peaks corresponding to CoGa or CoN were evident that might lead to inconsistent results. Therefore, it can be well recognized from diffraction patterns that

Co(lll) ions have successfully incorporated into the GaN lattice without changing the wurtzite crystal structure.

EDX Analysis:

Energy dispersive X-ray (EDX) analysis was carried out for determining the doping level of Co in GaN NNs. Prior to EDX measurement, sample surface was cleaned with ethanol to remove surface contamination and then dispersed on silicon wafers. It is clearly seen from EDX patterns, sharp peak indicates the presence of Ga and N contents. While small and wide peaks originate from Co elements. The analysis also provides the information of percentage by weight (wt%) and atomic percent (at%) of each element present which shows that these samples contain a specific stoichiometric amounts of Co, Ga and N. We also carried a complementary mapping, confirms that Co^{3+} ions are uniformly distributed in GaN matrix as shown in the Fig. S2(c).

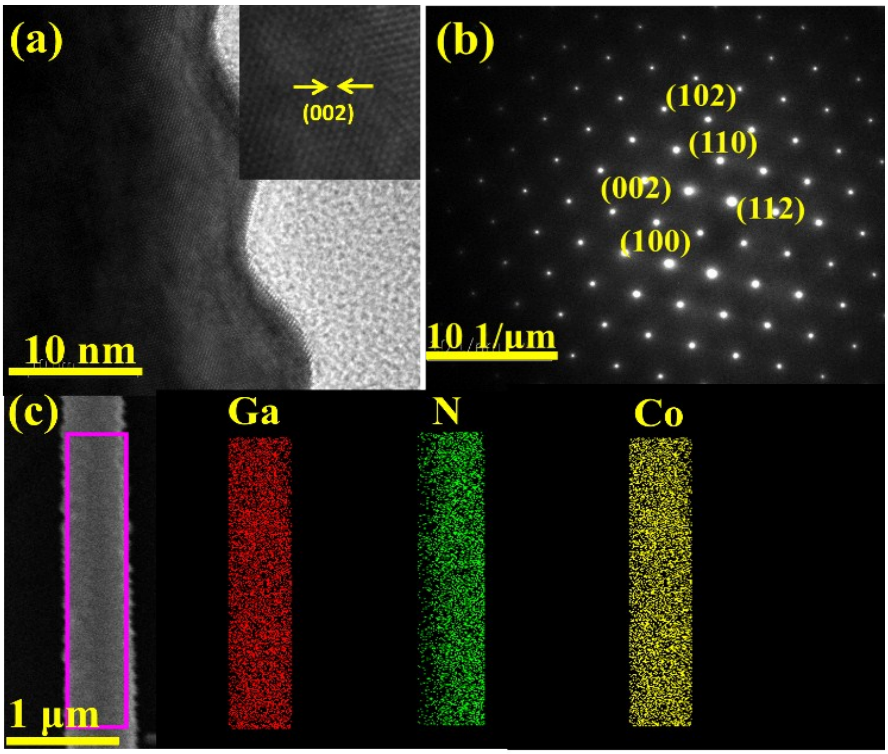

Figure S2. (a-b) HRTEM image of Co:GaN nanoneedles and its corresponding SAED pattern, (c) SEM mapping of Co-doped GaN nanoneedles.

It is obvious from HRTEM image that a clearly resolved lattice fringe was calculated to be 0.25 nm indicating the growth direction of nanoneedle is parallel to (002) plane of Co-implanted GaN nanoneedles, providing the evidence for the single crystalline growth of GaN NNs. The SAED pattern confirms the single crystalline nature of Co: GaN NNs, indicating well- defined spots as shown in Fig. S2(b). These spots are indexed to be (102), (110), (112), (002) and (110) planes which are in good agreement with XRD pattern.

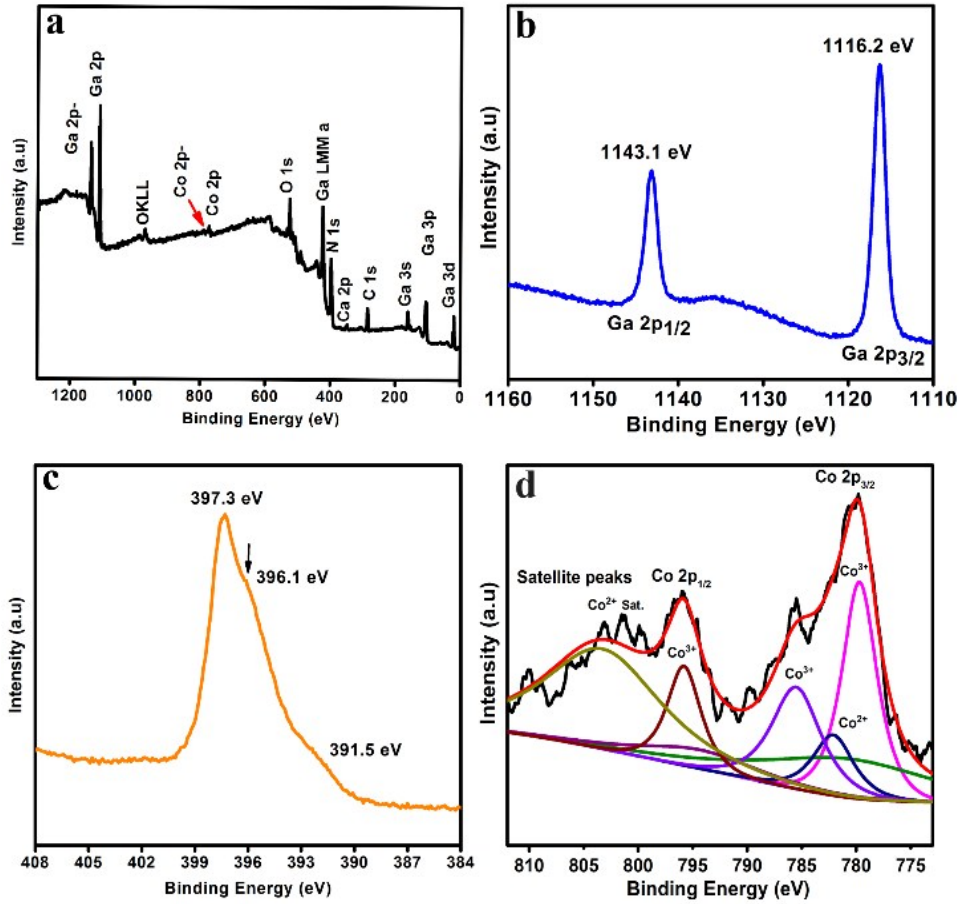

Figure S3. XPS survey spectra of Co-doped GaN NNs (a) Full spectrum, (b) Ga 2p, (c) N 1S, (d) Co 2p.

XPS analysis has been carried out to analyze the chemical bonding structure and valance state of a Co2p element in as-synthesis NNs. The survey spectrum of Co-doped sample is shown in Fig. S3(a) which confirms the presence of all the possible states of Ga, N, and Co with weak satellite peaks. In order to understand peak position clear, Gaussian fitting was employed on Co2p region indicates the contribution of heterovalent Co^{3+} and Co^{2+} cations. In the Co2p spectrum, the prominent peaks at 779.7 eV, 785.5 eV and at 795.8 eV correspond to valance states of Co^{3+} arises from the 3d-t_2g state below the Fermi level.[4-6] While, two other spin-orbit component, 2p3/2, and 2p1/2 states are observed at 782.1 eV and 803.3 eV which are attributed to Co^{2+} cations and Co^{2+} shake-up satellites, respectively.[7, 8] The spin energy separation of main Co 2p3/2 and Co 2p1/2 is observed to be 16 eV which is close to previous reports for Co_3O_4.[8] This suggested that Co2p is best fitted with two spin-orbit doublets which are characteristics of Co^{3+} and Co^{2+} with shake-up satellites. Similarly, the fine-scanned of N 1s is shown in Fig. S3(c), displays three visible peaks at 397.3 eV, 396.1 eV and 391.5 eV which are attributed to Ga-N bonding. The peak at the low energy side 391.5 eV of mainline of N 1s is not the intrinsic peak of N 1s, which is assigned to shakeup satellite peak due to the local carrier band within the bandgap of GaN. The binding energy of Ga has shifted by ~2 eV to lower binding energy as compared with as-grown nanowires presented by Lei *et al.*[9] This indicated the presence of strong interaction between cobalt species and GaN on the surface. The existence of Co^{2+}-Co^{3+} or Co^{3+}-Co^{3+} interaction with holes or charge state can give rise to the formation of magnetic polaron. This could be possible by superposition of weak ferromagnetic (FM) component into antiferromagnetic (AFM) component. Moreover, the XPS spectra also display the carrier effect in Co-doped GaN come from the N elements but not Ga, because there is no clear satellite peak in the spectra of Ga atoms.

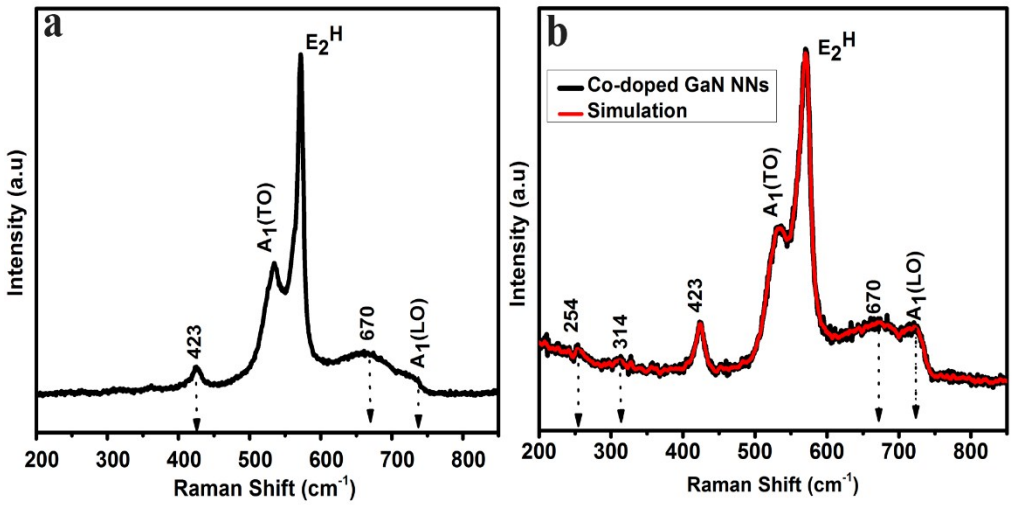

Figure S4. Micro-Raman spectrum of (a) Pure GaN and (b) Co-doped GaN nanoneedles.

High crystalline, defect-free Co-doped GaN nanowires have been synthesized by CVD. The typical micro-Raman spectrum of pure and Co-doped GaN nanostructures grown on mica substrate was collected at room temperature by using 532 nm laser as excitation source. We find that several vibrational modes associated with GaN Raman spectrum were detected at 531 cm^{-1}, 569 cm^{-1} and 720 cm^{-1} assigned to A_1(TO), E_2(High) and A_1(LO) where A_1 and E_2 are the Raman active modes as shown in (Fig. S4). Both spectrum indicate that observed phonon modes represent hexagonal wurtzite structure of GaN. Accordingly, strong peak in the undoped and Co-doped spectra is attributed to GaN nonpolar high-frequency optical phonon which is not influenced by carrier concentration because carrier effect in Co-doped GaN is dominant by N elements but not Ga, consistent with XPS results. It is also observed that when Co ions were incorporated into GaN lattice, A_1(LO) phonon mode significantly enhanced and shifted towards lower wave number of 716 cm^{-1}, compared with the undoped sample as shown in Fig. S4(b). This indicates the existence of phonon-carrier coupling with the A_1(LO) mode, caused by

defects. Here, Co ions doping didn't introduce the carriers in the lattice because of Co and Ga are in same valance state and no independent plasmon have been identified in the Raman spectra. So carrier plays a dominant role due to defects. On the other hand, observed broadened asymmetric line shape is a result of phonon confinement effect which softens and broaden Raman mode. With this, two additional peaks were observed at 314 cm^{-1} and 423 cm^{-1} that were assigned to an acoustic overtone of wurtzite GaN. The zone-boundary phonon (ZBP) at 254 cm^{-1} is activated by surface disorder and finite size effects. In general, quantum confinement gives rise the discrete energy levels in the nanocrystal, mainly attributed to orbital exchange interaction between d-level of dopant, p-level of the valence band and s-level of conduction band within the crystal.[10, 11] This analysis implies that residual stresses are presented in the sample where cobalt dopant plays dominant role. The comparative description of Raman modes of Co-doped GaN with previous reports is mentioned in Table S1.

Table S1. Phonon modes (cm^{-1}) and corresponding symmetries of strongest modes derived from Raman spectra of GaN and Co-doped GaN nanostructures.

Bulk GaN	As-grown Co-doped NWs/NNs	Pure GaN NW's	Symmetry	References
145			E_2 (low)	12, 13
	254		ZB Phonon	14
	314		Acoustic overtone	14
	423	423	Acoustic overtone	14
	531	531	A_1(TO)	12, 15, 16
533			A_1(TO)	12, 17, 18
569	569	569	E_2(high)	17-19
561			E_1(TO)	12
	670	670	ZB Phonon	20
	720		A_1(LO)	13
735-737		736	A_1(LO)	12-14
741-743, 745			E_1(LO)	12-14

ZFC-FC Measurement

Zero-field cooling (ZFC) and field cooling (FC) were measured at 200 Oe exhibit strong temperature dependence and their magnetic moments are gradually enhanced with decreasing temperature. The large separation between ZFC and FC magnetization curves is induced by the domain wall motion or competition between thermal energy and magnetic anisotropic energy rather than spin-glass-like transition.[21] After a careful analysis of both magnetization curves, nanoneedles exhibit clear humps or concave which indicate the complicated magnetism include mixed FM and AFM ordering in the sample. It is common that magnetic coupling pairs inside the host lattice may show their respective magnetic behaviors at different locations in a large size of crystals or wires. According to this, Co compounds are usually antiferromagnetic coupled materials if the dopant ions incorporated in pair with defect sites, whose T_C would be higher than 300K. In Co-doped GaN system, when the temperature is increased with the constant applied field in ZFC mode, magnetization rises to maximum, providing two maxima at 86 K and 335 K. A maximum at 335 K is referred as ordering temperature (T_C) which is defined as the temperature where $\frac{d\chi}{dT}$ has a maxium value, shown in the inset of (Fig. S5). This typical magnetic ordering has already been analysed for Mn-doped GaN where T_C is in the rang of 228–370 K.[22] While, A broad peak at 86 K, is an indication of FM-AFM transition that is found by coexistence of spin clustering (↑↑) and antiferromagnetic pairs coupling with N-vacancy or doped spin lead to a ferromagnetic character. In this mechanism, intrthe oduction of Co impurity substitute the Ga sites and may form the AFM pairs and a N-vacany site between them via exchange interaction. Then the charge transferred from Co ions to adjacent vacancies with spin like ↑ which forms (↓↑↑) cluster may give rise to FM behavior.[23] The transformation of AFM to FM ordering is related to localized carriers or defects, that rise up a clear an obvious hump in the ZFC curve at low temperature. The transition in such mechanism support the BMP formation due to free exciton (FX) coupling with TM ions.[24] Additionally, AFM-FM transition can also be manipulated by dipole-dipole interaction and coupling between spin polarized carriers by the applied

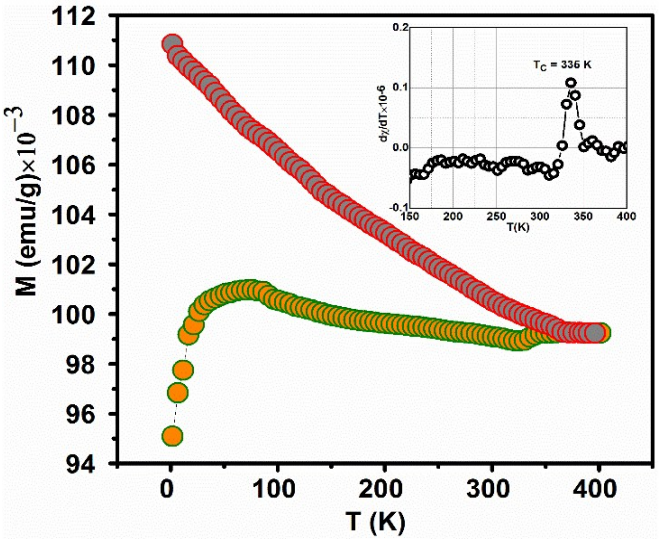

Figure S5. The ZFC and FC magnetization curves of Co-doped GaN NNs, inset shows clear view of Curie temperature for GaN:Co NNs.

Magnetic Reversal Mechanism in Co-doped GaN NNS

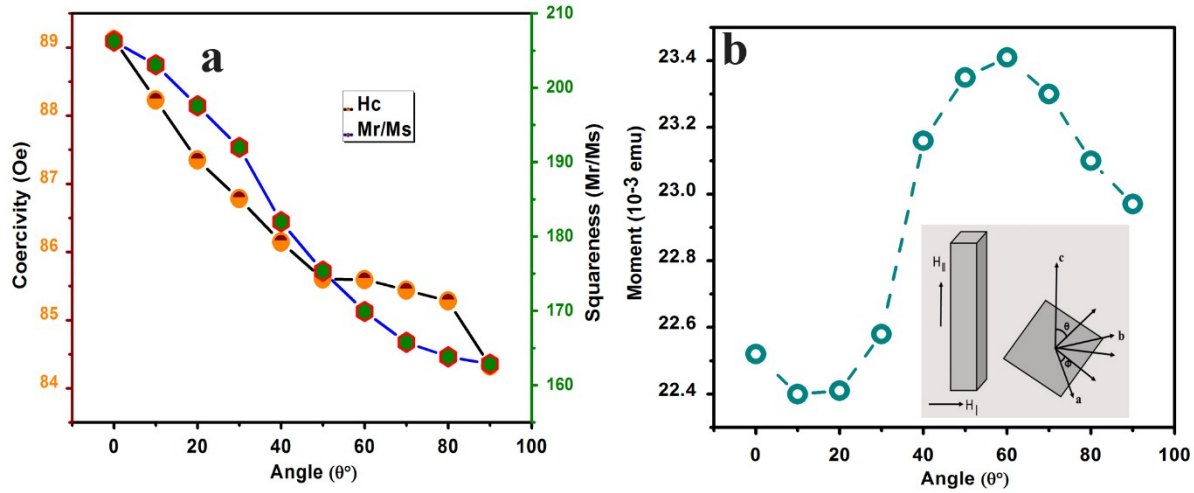

Figure S6. (a) Angular dependence of Hc and Mr/Ms in the range of 0° to 90°, (b) Angular dependence of magnetization for 0° ≤ θ≤ 90°, where θ is the angle between magnetization and wire axis (*c*-axis) and φ is the angle between in-plan projection of magnet.

The exchange of spin angular momentum between the conduction electrons and local magnetization provides an efficient means of controlling spins of nanostructures and has potential applications toward memory, logic and microwave devices.[25] In order to confirm easy axis to lie parallel or perpendicular to the wire axis, angular dependence of squareness (Mr/Ms) is determined as shown in Fig. S6(a). Initially, $H_C(\theta)$ and $S(\theta)$ both decreases monotonically, attain maximum value at $\theta = 0°$ and minimum value at $\theta = 90°$ which indicates easy of magnetization along NW's/NNs and hard axis perpendicular to NNs axis. According to magnetization reversal mechanism of nanowires, coercivity increases as the angle increase, dominant curling mode with lowest H_C at $\theta = 0°$ and highest H_C value at $\theta = 90°$. On the other hand, decreases of coercivity with increase of polarization direction from 0° to 90° can give rise the coherent rotation mode.[26] In this study, H_C initially decreases with increase of angular rotation but a significant transition occurs at above $\theta = 40°$ called critical angle, it starts to increase slightly. This transition

from coherent mode to curling mode with increasing polarization rotation is the characteristics of domain wall motion in which magnetic impurity induces exchange-coupling with neighboring column.[27] This result further confirms the coexistence of ferromagnetic (FM) and antiferromagnetic (AFM) order in Co-doped GaN NNs and allow current-induced magnetization switching (CIMS) precession which could be useful for design of memory devices based on nanostructures. Mainly, the spin orientation strongly depend on polar direction and diameter of nanowire due to overlap of orbitals and thus exchange interaction is changed.[28] Since the length and diameter of as-synthesized nano-needles are much larger than critical value i.e d = ≥ 200nm, magnetic moment will align perpendicular to needles axis for larger angle can give rise to coherent rotation mode and align parallel to NN's axis for small angles then curling mode is present which are in good agreement with previous report.[29] The magnetic polarization in Co-doped NNS strongly is relatively complicated mechanism strongly depend on local magnetic moment. The major contribution to align the local magnetic moment along the easy axis is expected to be magnetocrystalline anisotropy and dipole-dipole interaction. This observation is based on the understanding of local emission spectrum. The local magnetic moment is formed when FX can combine with ferromagnetic TM ion pair (↑↑) by exchange interaction to form EMP, then the magnetic anisotropy could originate in magnetocrystalline anisotropy or pair orientation, usually close to the growth direction. While BMP is formed by local carrier or defect involve AFM ion pair or cluster coupled with FX behave as strong magnetic moment because of strong magnetic coupling between atom in the same cluster, both of them can be identified in the PL spectra with obvious intensities. For BMP formation, the charges polarize in perpendicular to *c*-axis as indicated by its Raman spectra, so its induced magnetic polarization should be parallel to *c*-axis. Therefore, the combined magnetic polarization due to different magnetic polaron in Co-doped GaN nanowire is very along to *c*-axis. Recently, Zou *et al.* reported photoinduced EMP transition in diluted Mn-doped $CH_3NH_3PbBr_3$ has narrow spin polarization emission for 25-30° rotation but not 45°, this indicates there may not be complete dependence on the rod axis because EMP contains spin polarization nature, however, it has long axis LO phonon coupling[30] so still exhibit *c*-axis dependence, similar to our results. In DMS nanowire like GaN: Co, the diluted dopants can produce several

local magnetic moments within nanowire which could not contribute collectively to exhibit shape anisotropy. However, the magnetic dipole-dipole interaction between Co dopant and host lattice should take part to do so in the presence of applied field. If the local magnetic moment can align then dipole-dipole interaction can be ferromagnetic.[31] Therefore, it is concluded that net magnetic anisotropy is determined by the local contributions of magnetocrystalline anisotropy and dipole-dipole interaction anisotropy in this NNS along easy axis of magnetization.

The trend of saturation magnetization with respect to angle is shown in Fig. S6(b). It is clearly noticeable that saturation field increases with rotation of axis, achieved a maximum value at $\theta = 90°$ correspond to the easy axis than perpendicular to the wire long axis. Above this, moment gradually starts decreasing by further rotation. This type of fashion is a typical signature of BMPs presents within the system.

References:

1. G. Nabi, C. Cao, W. S. Khan, S. Hussain, Z. Usman, M. Safdar, S. H. Shah and N. A. D. Khattak, *Applied Surface Science*, 2011, **257**, 10289-10293.
2. T. I. Shin, H. J. Lee, W. Y. Song, H. Kim, S. W. Kim and D. H. Yoon, *Colloids and Surfaces A: Physicochemical and Engineering Aspects*, 2008, **313-314**, 52-55.
3. C.-Y. Nam, D. Tham and J. E. Fischer, 2007.
4. M. C. Biesinger, B. P. Payne, A. P. Grosvenor, L. W. Lau, A. R. Gerson and R. S. C. Smart, *Applied Surface Science*, 2011, **257**, 2717-2730.
5. W. Guo, Y. E, l. Gao, L. Fan and S. Yang, *Chemical Communications*, 2010, **46**, 1290-1292.
6. H. Che, A. Liu, J. Hou, J. Mu, Y. Bai, S. Zhao, X. Zhang and H. He, *Journal of Materials Science: Materials in Electronics*, 2014, **25**, 3209-3218.
7. B. Ernst, S. Libs, P. Chaumette and A. Kiennemann, *Applied Catalysis A: General*, 1999, **186**, 145-168.
8. L. Fu, Z. Liu, Y. Liu, B. Han, P. Hu, L. Cao and D. Zhu, *Advanced Materials*, 2005, **17**, 217-221.
9. M. Lei, H. Yang, P. Li and W. Tang, *Applied Surface Science*, 2008, **254**, 1947-1952.
10. W. Zheng, P. Kumar, A. Washington, Z. Wang, N. S. Dalal, G. F. Strouse and K. Singh, *Journal of the American Chemical Society*, 2012, **134**, 2172-2179.
11. D. Ortega Ponce, CRC PressI Llc, 2012.
12. C.-C. Chen, C.-C. Yeh, C.-H. Chen, M.-Y. Yu, H.-L. Liu, J.-J. Wu, K.-H. Chen, L.-C. Chen, J.-Y. Peng and Y.-F. Chen, *Journal of the American Chemical Society*, 2001, **123**, 2791-2798.
13. J. Jian, X. Chen, Q. Tu, Y. Xu, L. Dai and M. Zhao, *The Journal of Physical Chemistry B*, 2004, **108**, 12024-12026.
14. U. Rössler, *Landolt Börnstein*, 2011.
15. G. Cheng, L. Zhang, Y. Zhu, G. Fei, L. Li, C. Mo and Y. Mao, *Applied Physics Letters*, 1999, **75**, 2455-2457.
16. J. Zhang and L. Zhang, *Journal of Physics D: Applied Physics*, 2002, **35**, 1481.
17. H. Siegle, G. Kaczmarczyk, L. Filippidis, A. Litvinchuk, A. Hoffmann and C. Thomsen, *Physical Review B*, 1997, **55**, 7000.
18. C. Wetzel and I. Akasaki, 1998.
19. Y. Xu, B. Yao and Q. Cui, *RSC Advances*, 2016, **6**, 7521-7526.
20. W. Gebicki, J. Strzeszewski, G. Kamler, T. Szyszko and S. Podsiadło, *Applied Physics Letters*, 2000, **76**, 3870-3872.
21. T. T. Gurgel, M. Buzinaro and N. Moreno, *Journal of superconductivity and novel magnetism*, 2013, **26**, 2557-2559.
22. M. Reed, N. El-Masry, H. Stadelmaier, M. Ritums, M. Reed, C. Parker, J. Roberts and S. Bedair, *Applied Physics Letters*, 2001, **79**, 3473-3475.
23. G. Chang, E. Kurmaev, D. Boukhvalov, L. Finkelstein, S. Colis, T. Pedersen, A. Moewes and A. Dinia, *Physical Review B*, 2007, **75**, 195215.
24. L. Hou, L. Pan, B. Liang, Y. Liu, L. Zhang, A. Bukhtiar, L. Shi, R. Liu and B. Zou, *Nanotechnology*, 2018, **29**, 055707.

25. H.-W. Lee and H. Yang, *Journal of Magnetics*, 2011, **16**, 92-96.
26. M. Irfan, U. Khan, W. Li, N. Adeela, K. Javed and X. F. Han, *Materials Letters*, 2016, **180**, 235-238.
27. M. Sawicki, F. Matsukura, A. Idziaszek, T. Dietl, G. Schott, C. Ruester, C. Gould, G. Karczewski, G. Schmidt and L. Molenkamp, *Physical Review B*, 2004, **70**, 245325.
28. M. Hegde, S. S. Farvid, I. D. Hosein and P. V. Radovanovic, *ACS Nano*, 2011, **5**, 6365-6373.
29. X. F. Han, S. Shamaila, R. Sharif, J. Y. Chen, H. R. Liu and D. P. Liu, *Advanced Materials*, 2009, **21**, 4619-4624.
30. Z. Shuangyang, G. Zhihong, L. Bianbian, H. Lipeng, L. Ruibin, Z. Haizheng, Z. Bingsuo and A. V. Kavokin, *Journal of Physics Communications*, 2017, **1**, 055018.
31. T. Fukushima, K. Sato, H. Katayama-Yoshida and P. H. Dederichs, *Japanese journal of applied physics*, 2006, **45**, L416.